



# Near-ideal absorption high oblique incident angle stable metamaterial structure for visible to infrared optical spectrum applications

Md. Bakey Billa<sup>1</sup> · Mohammad Lutful Hakim<sup>1</sup> · Touhidul Alam<sup>1</sup> · Ali F. Almutairi<sup>2</sup> · Norbahiah Misran<sup>3</sup> · Mohamed S. Soliman<sup>4,5</sup> · Mohammad Tariqul Islam<sup>3</sup>

Received: 3 July 2023 / Accepted: 11 September 2023 / Published online: 3 October 2023  
© The Author(s), under exclusive licence to Springer Science+Business Media, LLC, part of Springer Nature 2023

## Abstract

The Metamaterial Absorber (MA) has emerged as a game-changing tool for various applications such as photodetectors, plasmonic sensors, energy harvesting, imaging, solar cells, optical modulators, and more. The proposed square enclosed square resonators metamaterial comprises single layer metal-dielectric-metal structure (Ni–SiO<sub>2</sub>–Ni) to achieve over 90% absorption bandwidth from 360 to 1750 nm. The average absorption at the operational wavelength is 94.47%, and a peak absorption of 99% appears at 900 nm. The designed MA shows polarization insensitivity and oblique incident angle stability up to 60°. Parametric design analysis, electric field, magnetic field, surface current distribution, and temperature distributions have been investigated to comprehend the absorption characteristics of the MA. The Polarization Conversion Ratio result shows the proposed MA as a perfect absorber rather than a polarization converter. The effect of concave and convex bending has also been investigated up to 16°, validating the stable absorption behavior. Finally, the designed MA can be a potential candidate for visible and optical window applications such as solar energy harvesting, photodetectors, light trapping, etc.

**Keywords** Metamaterial absorber · Energy harvesting · Oblique incident angle stability · Polarisation insensitive · Visible and optical window · Bendable

---

✉ Touhidul Alam  
touhidul@ukm.edu.my

✉ Mohammad Tariqul Islam  
tariqul@ukm.edu.my

<sup>1</sup> Pusat Sains Angkasa (ANGKASA), Institut Perubahan Iklim, Universiti Kebangsaan Malaysia (UKM), 43600 UKM Bangi, Selangor, Malaysia

<sup>2</sup> Abdullah Al Salem University (AASU), Khaldiya, Kuwait

<sup>3</sup> Department of Electrical, Electronic and Systems Engineering, Faculty of Engineering and Built Environment, Universiti Kebangsaan Malaysia (UKM), 43600 UKM Bangi, Selangor, Malaysia

<sup>4</sup> Department of Electrical Engineering, College of Engineering, Taif University, PO Box 11099, Taif 21944, Saudi Arabia

<sup>5</sup> Department of Electrical Engineering, Faculty of Energy Engineering, Aswan University, Aswan 81528, Egypt

## 1 Introduction

Metamaterial is an artificially engineered material not found in nature and has unusual or beyond-the-ordinary effects on electromagnetic (EM) waves. The applications of metamaterial are widely adopted in different fields like absorbers (Liu et al. 2021), cloaking (Dash et al. 2016), antennas (Alam et al. 2021; Hakim 2022), energy harvesters (Byrnes et al. 2014), super lenses (Tang et al. 2021), photodetectors (Ponizovskaya Devine 2021), sensors (Hakim et al. 2022a; Karthikeyan et al. 2022; Bazgir et al. 2022; Razavi and Zarrabi 2022), reflect array (Misran et al. 2012), bio-sensor (Farmani et al. 2018) and modulators (Carrillo et al. 2016), etc. The initial concept of a perfect metamaterial absorber is proposed by Landy et al. (2008); after that, substantial research interest has increased in this arena, and many researchers have started to explore details about metamaterial absorbers for numerous applications in different wavelengths like optical, infrared (IR) (Bazgir 2023; Mobasser et al. 2021), visible, microwave, and terahertz (THz) spectra (Poorgholam-Khanjari and Zarrabi 2021; Zarrabi et al. 2019). Generally, MA absorbers can be classified into two categories: (i) narrow-band MA and (ii) wide-band MA. Narrow-band MAs have shown excellent performance in sensing and filtering (Bilal et al. 2022). On the other hand, wide-band MAs are widely used in stealth technology (Yin et al. 2015), radar cross-section reduction (RCSR) (Mehrabi et al. 2019), photovoltaics, thermal emitters (Tang et al. 2020), etc. In recent years, various MAs have been developed and investigated for single, dual, multi, and wideband applications at different operating frequencies (Ning et al. 2022; Ding et al. 2012), and broadband metamaterial absorber by multiple stacked layers or multi-resonator metamaterial-based structures (Yin et al. 2015; Ding et al. 2012).

Recently, EM wave absorbers have been significantly utilized in the ultraviolet (UV), infrared (IR), and visible bands due to their unparalleled interest in their application of photovoltaics, thermal emitters, and energy harvesting (Mehrabi et al. 2019; Naveed et al. 2021; Bilal et al. 2020). An optical wavelength (300–680 nm) MA is designed with a larger dimension of  $1555 \times 1555 \times 560 \text{ mm}^3$ , with low incident angle stability and absorption (Chen et al. 2023). A numerical study of metamaterial absorber is presented in Hakim et al. 2022a for visible optical wavelength where the unit cell size of the MA is reduced to  $950 \times 950 \times 240.13 \text{ mm}^3$ , and incident angle stability and average absorption are increased by  $60^\circ$  and  $92.2\%$ , respectively. Another sun-shaped resonator-based MA is designed with three layers of materials covering the only visible region 390–760 nm (Shuvo et al. 2021). Besides, some researchers have proposed MA for covering the visible-to-infrared optical regime (Tian et al. 2023; Zhang et al. 2021). For example, a broadband MA operated in the visible to infrared optical spectrum (405–1505 nm) with incident angle stability of  $60^\circ$  and polarization-insensitive characteristics; however, the MA shows a high thickness of 415 nm due to the four layers (Zhang et al. 2021). A three-layer MA is presented in Musa et al. (2022), which shows low incident angle stability of only  $45^\circ$ . Similarly, another three-layer MA also shows only  $45^\circ$  incident angle stability, and the average absorption is less than 90%. The bending of the MA is also an important issue during the installation; however, except (Hakim et al. 2022a), the research work in Chen et al. (2023) (Zhang et al. 2021) (Musa et al. 2022) (Li et al. 2022) does not show the bending investigation. Despite all this research, there is still a high demand for an MA with a wide operating wavelength (visible to infrared), high incident angle stability, and low thickness capable of bending tolerance.

Therefore, a single-layered (Ni-SiO<sub>2</sub>-Ni) multiple resonator-based MA is designed in this research for visible to infrared optical spectrum with lower dimensions ( $200 \times 200 \text{ mm}^2$ ) and

a thickness of 75 mm only, capable of bending tolerance. The proposed MA shows 94.47% average absorption from 360–1750 nm and incident angle stability of up to 60°. Additionally, the symmetrical structure of the developed MA achieved polarization insensitivity for both Transverse Electric (TE) and Transverse Magnetic (TM) modes.

## 2 Metamaterial absorber design

The proposed MA structure consists of single layer sandwich configuration (Ni-SiO<sub>2</sub>-Ni), illustrated in Fig. 1. The resonator (Ni) and base (Ni) layers have been placed face-to-face, and a single dielectric substrate (SiO<sub>2</sub>) is inserted between them. Nickel material is chosen due to its attractive features like abundant solar absorber material for low-temperature solar-to-thermal energy conversion systems, the higher electrical conductivity of  $1.44 \times 10^7$  S/m, and availability (Garrison 1984). On the other hand, SiO<sub>2</sub> is used as a dielectric insulator because of its high optical transparency and relative permittivity, chemical stability, relatively thinness, and high-level breakdown voltage (Kumar et al. 2022). The loss tangent ( $\tan\delta$ ) and dielectric constant ( $\epsilon_r$ ) of SiO<sub>2</sub> are 0.0004 and 3.8, respectively. The top resonators structure and its symmetricity play a key role in achieving close-to-unity absorption and polarisation-insensitive characteristics (Xiong et al. 2022). The overall dimension of the designed MA is  $200 \times 200 \times 75$  nm<sup>3</sup>, and all design parameters are listed in Table 1.

The proposed MA is designed and simulated using commercially available CST Microwave Studio software (CST Studio Suite xxxx). The unit cell boundary conditions are employed along the x-axis and y-axis, respectively and open add space boundary conditions are in the z-axis (along with the wave propagation direction). The excitation is provided by using floquet port along the z-axis. The absorption value ( $A$ ) is obtained through Eq. (1), where  $S_{11}$  is the reflection coefficient, and  $S_{21}$  is the transmission coefficient of MA (Mehrabi et al. 2019; Hakim et al. 2022b).

$$A(\lambda) = 1 - |S_{11}|^2 - |S_{21}|^2 \quad (1)$$

The value of  $S_{11}$  and the  $S_{21}$  of the absorber can be derived using Eqs. (2) and (3) (Chen et al. 2004).

$$S_{11} = \frac{R_{01}(1 - e^{i2nk_0d})}{1 - R_{01}^2 e^{i2nk_0d}} \quad (2)$$

$$S_{21} = \frac{(1 - R_{01}^2)e^{ink_0d}}{1 - R_{01}^2 e^{i2nk_0d}} \quad (3)$$

where  $R_{01} = z - 1/z + 1$ ,  $z$  is impedance, and  $n$  is the refractive index obtained by inverting Eqs. (2) and (3), yielding (Chen et al. 2004).

$$z = \pm \sqrt{\frac{(1 + S_{11})^2 - S_{21}^2}{(1 - S_{11})^2 - S_{21}^2}} \quad (4)$$

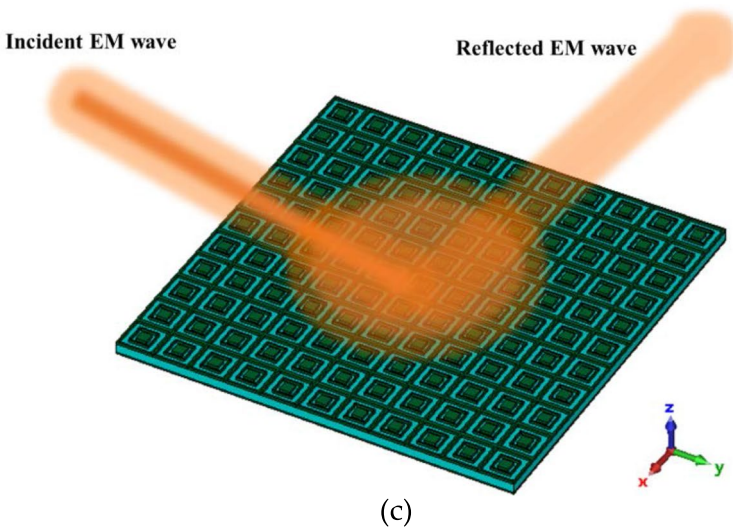
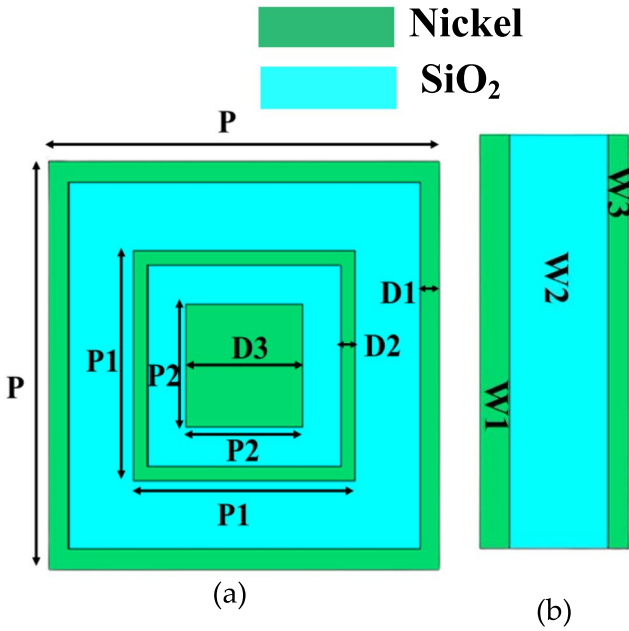


**Fig. 1** MA array perspective view, the unit cell design **a** front view, **b** side view, and **c** array perspective view

$$n = \frac{1}{K_0 d} \{ [\ln(e^{ink_0 d})] + 2m\pi - i[\ln(e^{ink_0 d})] \} \quad (5)$$

The "m" is an integer number that correlates to the real refractive index value. In the above Eqs. (5), "k<sub>0</sub>" and "d" denote the absorber's wave number and thickness,

**Table 1** Parameters value of the designed MA

Parameters	Value (nm)	Parameters	Value (nm)
P	200	D1	10
P1	113.14	D2	7.075
P2	60	D3	30
W1	10	W2	50
W3	15		

respectively. To achieve maximum absorption, ( $S_{21}$ ) and ( $S_{11}$ ) should be kept as low as possible. The bottom nickel sheet behaves as an ideal reflector and completely blocks transmission, resulting in  $S_{21}=0$ . Therefore, the incoming wave becomes trapped in the dielectric substrate. The absorption can also be expressed in terms of S-parameters using the Eq. (6) (Naveed et al. 2021).

$$A(\lambda) = 1 - |S_{11}|^2 \quad (6)$$

Equation (5) shows that if the absorption value needs to increase, the value of  $S_{11}$  must be as low as possible. The value of  $S_{11}$  will be low if the free space impedance matches with the MA effective impedance  $z(\omega) = \text{Re}(z) + \text{Im}(z)$ , Which can be understood by equating the Eqs. (4) and (6). In Eq. (7), the near unity value of the real part and near-zero value of the imaginary part will provide near unity absorption.

$$A(\lambda) = \frac{4\text{Re}(z)}{[1 + \text{Re}(z)]^2 + [\text{Im}(z)]^2} \quad (7)$$

The input impedance depends on the metamaterial structure's effective permittivity and permeability, calculated by Nicolson Ross Weir's (NRW) equation (Rothwell et al. 2016). The effective impedance of MA, also related to the relative permittivity ( $\epsilon_r$ ) and the relative permeability ( $\mu_r$ ) of the medium, are calculated using Eqs. (8) and (9) (Chen et al. 2004; Smith et al. 2002). Where  $Z$  is the effective impedance,

$$\epsilon_r = \frac{n}{Z} \quad (8)$$

$$\mu_r = nZ \quad (9)$$

The absorption, reflectance, and transmittance of the proposed MA is illustrated in Fig. 2a. The simulated absorption of the designed MA is found to be more than 90% in the wavelength range of 360 nm to 1760 nm. The average absorption is 94.47% from 360 to 1760 nm with a peak absorption is 99.42% at 900.8 nm wavelength. The high absorption mechanism of the proposed MA is explained using design evolutions. The design evolution of multiple resonators and corresponding absorption is shown in Fig. 2b. Initially, the inner square patch resonator achieves absorption at higher wavelength regions and low absorption at visible regions. After that, the middle ring is incorporated to create the electromagnetic coupling between the inner and middle resonator, which increases significant absorption at the middle operational wavelength of MA, illustrated in Fig. 2c. Besides, the absorption value increases at the entire operational wavelength. The absorption is further improved at visible wavelength by incorporating

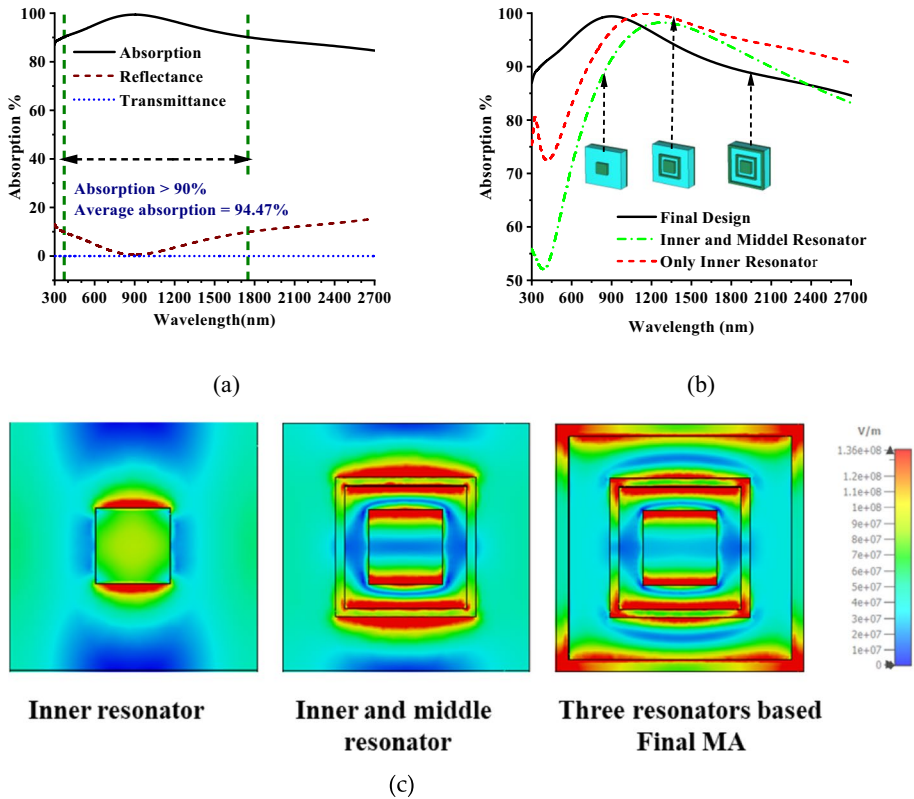


**Fig. 2** **a** Absorption, reflectance, and transmittance curve of proposed MA, **b** absorption improvement of MA for multiple resonators, and **c** e-filed coupling by different resonator configurations at 300 nm wavelength

the outer resonator due to the more coupling effect by three resonators. The electric and magnetic fields of the different resonator configurations are presented in Fig. 2c

The structural parameters also play a crucial role in achieving high absorption. In Fig. 3, the absorption level is analyzed by varying the geometrical parameter values of the MA. In Fig. 3a, the absorption value is investigated for different values of  $W1$  with 2 nm intervals while the additional parameters remained constant. No significant influence is observed for changes in the value of  $W1$ . This is because of the absorption of electromagnetic waves in a metamaterial is primarily determined by the properties of the metamaterial itself, such as its composition, structure, and dimensions, rather than the thickness of the ground plane. Figure 3b represents the absorption of different dielectric thicknesses ( $W2$ ). The value of  $W2$  is changed from 50 to 70 nm with a 10 nm interval, and it is noticed that with the increases of  $W2$ , the rate of absorption increased. If the dielectric layer is thick, the absorption of electromagnetic waves in the metamaterial may be enhanced. This is because the waves must pass through the dielectric layer multiple times, allowing for multiple interactions between the waves and the metamaterial structure. This results in increased absorption of the electromagnetic waves in the metamaterial. But the higher value of  $W2$  increased size, weight, fabrication complexity, and reduced bandwidth. For better efficiency,  $W2$  is adjusted to 50 nm.

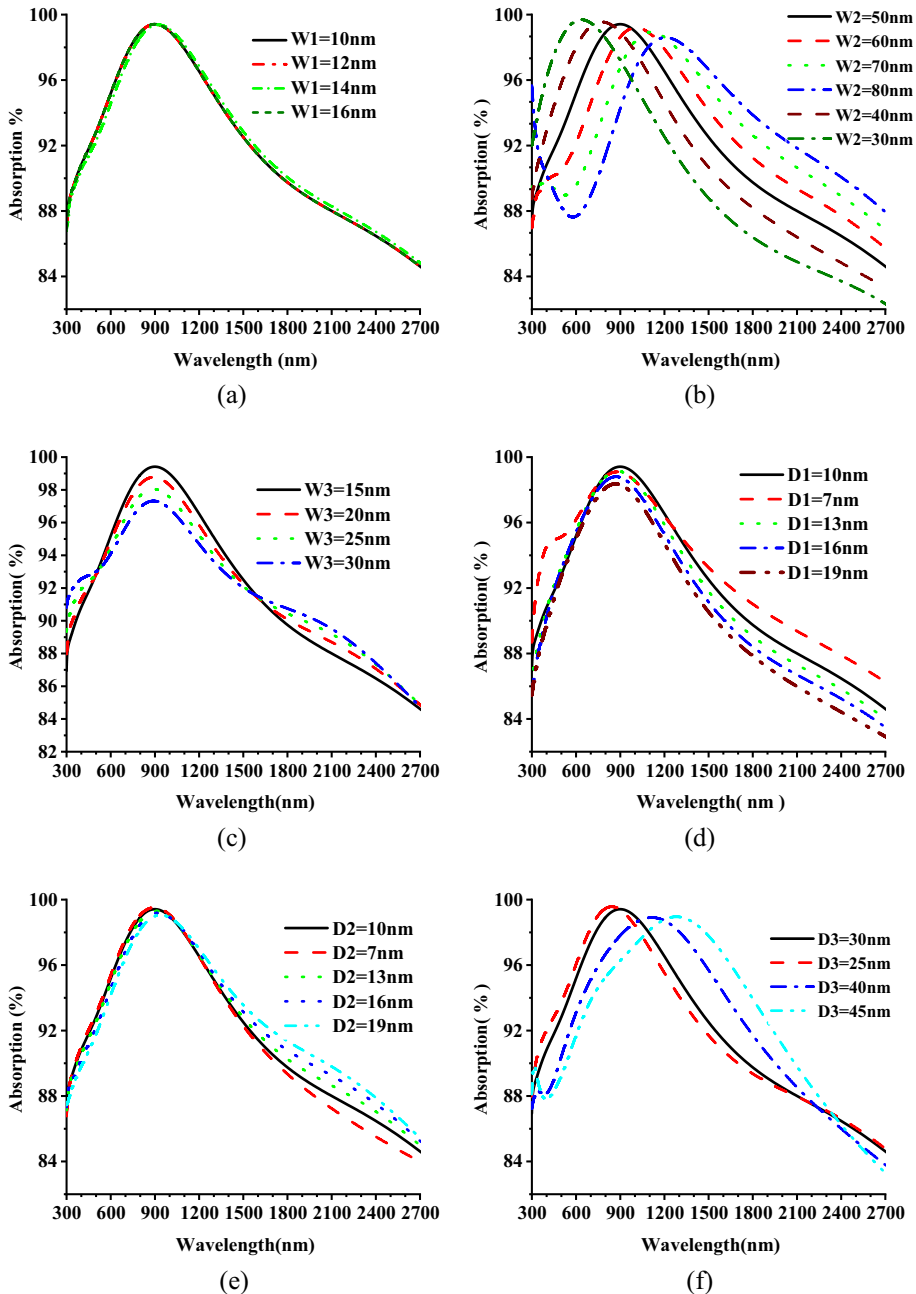


**Fig. 3** Absorption analysis for different values of: **a** Ground thickness ( $W_1$ ), **b** Dielectric thickness ( $W_2$ ), **c** Top layer thickness ( $W_3$ ), **d** Outside square wide ( $D_1$ ), **e** Middle square wide ( $D_2$ ), and **f** Centre solid square wide ( $D_3$ )

In Fig. 3c, the patch thickness of the MA is studied for  $W3$ , and a continual trend is noticed for various  $W3$  values with almost no significant contribution to the variation of MA absorption. The outer square width ( $D1$ ) is altered from 7 to 19 mm while all other parameters remained constant. Figure 3d shows the effect of changing the width ( $D1$ ) on the absorption curve. As  $D1$  increases, the absorption curve slightly decreases, and at 10 mm, the MA shows better absorption than others. On the other side, the middle square side ( $D2$ ) is also changed in the same manner from 7 to 19 mm, and the curve slightly decreased in the lower wavelength but slightly increased in the upper wavelength, as illustrated in Fig. 3e. Finally, the center solid square width ( $D3$ ) is changed from 25 to 45 mm, while all other parameters remain constant. The absorption curve slightly decreases from 300 to 1200 nm wavelength and slightly increases in the upper wavelength region. For better average absorption,  $D3$  is adjusted to 15 nm. The absorption effect by different layers is presented in Fig. 4. The only dielectric shows near zero absorption because it transmits all incident EM waves. The combination of resonator layers and dielectric layers improves the absorption at the desired wavelength. Finally, the completed metal-based layers block the transmission of EM waves and increase the absorption level.

### 3 Results and discussions

#### 3.1 Metamaterial property

The absorption behavior depends on the impedance matching of the designed MA. The relative impedance ( $Z$ ) matching of the designed MA is calculated by using Eq. (9) (Cen et al. 2020) and Fig. 5a illustrates the relative impedance of both TM and TE modes. The close-to-unity value of the real part and close to the null value of the imaginary part indicates that the proper effective impedance of the designed MA matches with the free space impedance, which approaches a greater level of absorption.

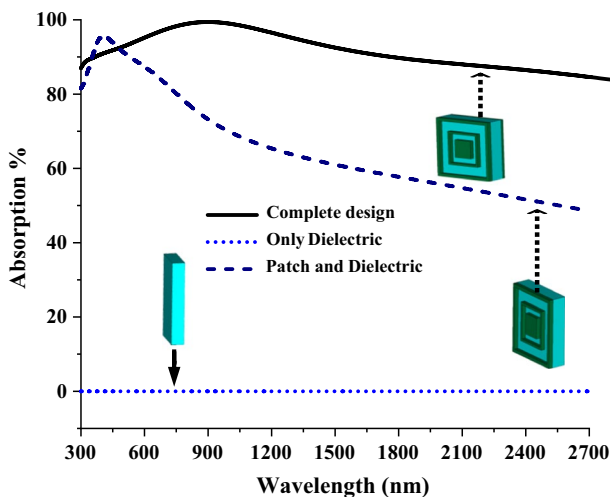
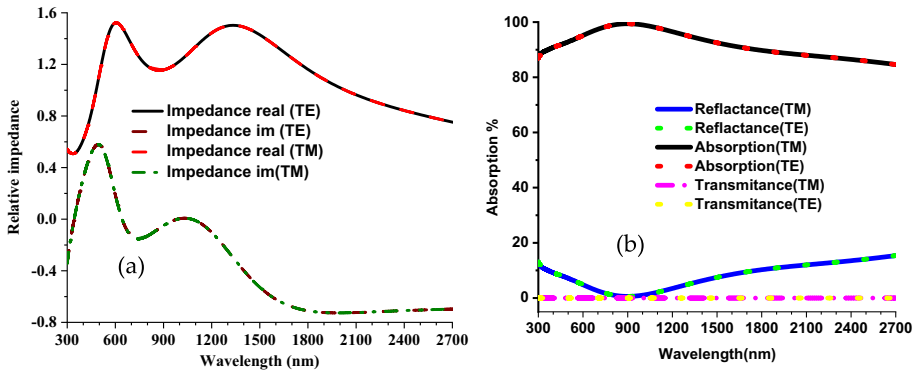


Fig. 4 The designed MA's absorption for different layers





**Fig. 5** **a** Relative impedance curves (TM and TE mode), **b** Absorption **a**, reflectance(R), and Transmittance(T) curves (both TE and TM mode)

$$Z = \sqrt{(1 - S_{11})^2 - S_{21}^2} / (1 - S_{11})^2 - S_{21}^2 = \sqrt{\mu/\epsilon} / z_0 = \sqrt{\mu_r/\epsilon_r} \tag{9}$$

where,  $\mu = \mu_r \mu_0$  is the permeability of the MA, and  $\epsilon = \epsilon_r \epsilon_0$  is the permittivity.  $\epsilon_0$  and  $\mu_0$  denotes the vacuum space permittivity and permeability, respectively. On the other hand, the free space impedance is denoted by  $Z_0$  where  $Z_0 = \sqrt{\mu_r/\epsilon_r}$ .

### 3.2 Polarization-conversion ratio (PCR)

The value of PCR is calculated to make sure that the designed MA is not a polarisation converter. Figure 6a shows the cross-polarisation reflection  $r_{xy}$  and the co-polarisation reflection  $r_{yy}$  is nearly zero in linear magnitude. Co—and cross-polarisation has defined as the Eq. (10) and (11), respectively (Chen et al. 2015),

$$r_{xy} = |E_{xr}/E_i|^2 \tag{10}$$

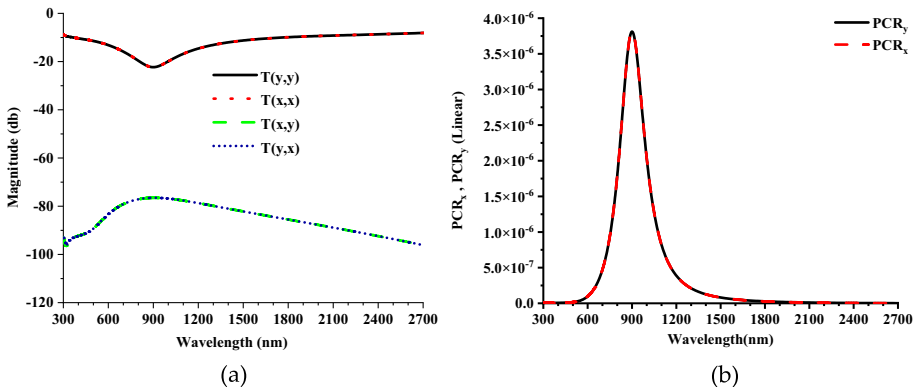


**Fig. 6** **a** Co and cross-polarisation, **b** PCR value (x to y and y to x) incident wave

$$r_{yy} = \left| E_{yr} / E_i \right|^2 \tag{11}$$

Thus, the polarisation-conversion ratio (PCR) is calculated by Eqs. (12) and (13) (Xiao et al. 2015).

$$PCR_y = T_{xy}^2 / (T_{yy}^2 + T_{xy}^2) \text{ for Y to , X polarised wave} \tag{12}$$

$$PCR_x = T_{yx}^2 / (T_{xx}^2 + T_{yx}^2) \text{ for X to , Y polarised wave} \tag{13}$$

Where  $T_{xx}^2 = T_{yy}^2$  is X- polarisation reflectivity and  $T_{yx}^2 = T_{xy}^2$  is Y-polarization reflectivity. Figure 6 shows the simulated result of PCR versus wavelength and polarisation versus wavelength. It ensures that this designed MA has not converted the wave. In Fig. 6b, The PCR value is shown, and it can be noticed that near zero value. So, it certifies that the designed MA is an absorber, not a polarisation converter.

Figures 7 represents the material property of the relative permittivity ( $\mu_r$ ), and relative permeability ( $\epsilon_r$ ), in both TE and TM modes, respectively. The  $\mu_r$  and  $\epsilon_r$  depend on the S-parameters. Therefore, Eqs. (7) and (8) give the normalized effective impedance of the surface. The real value of effective impedance is approaching unity over a large visible and optical regime which verifies the impedance match among the MA structure and free space. Hence, the designed MA demonstrates an average absorption level of 94.47% from 360 to 1750 nm.

### 3.3 Polarization insensitivity and oblique incident angle stability

The polarisation insensitivity of the designed MA is also evaluated to establish the absorption capability. Figure 8 indicates the oblique angle ( $\theta$ ) and the polarisation angle ( $\varphi$ ) on the EM wave. Here EM wave propagated towards the negative z-axis. The blue sphere shows the  $360^\circ$  phi ( $\varphi$ ) angle area of the EM wave, and the green half-sphere indicates the  $180^\circ$  oblique incident-angle area of EM wave theta ( $\theta$ ) angle area of EM wave components such as electric and magnetic field vectors. The absorption property of the various

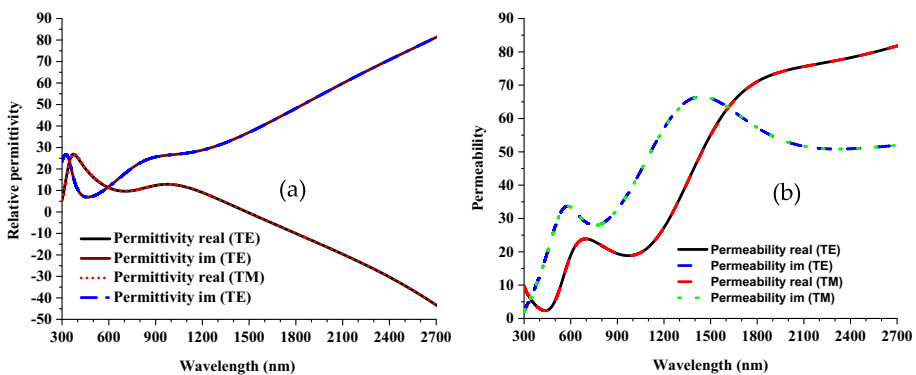
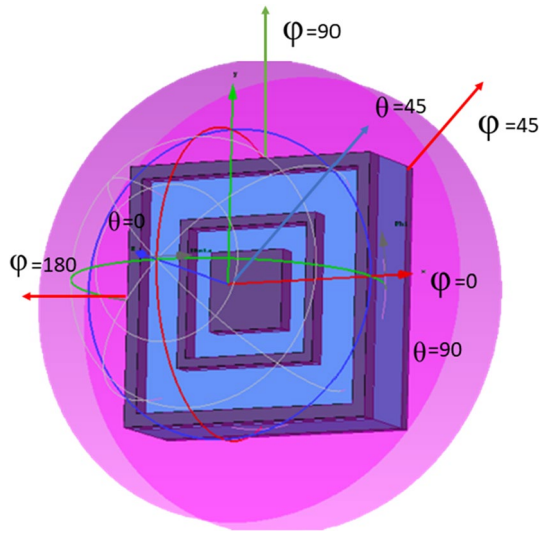


Fig. 7 Metamaterial properties of the MA at both TE and TM mode of a relative permittivity b relative permeability

**Fig. 8** Pointing of ( $\varphi$ ) and ( $\theta$ ) incident angle of EM wave on designed MA



polarisation incident angle ( $\varphi$ ) and oblique incident angles ( $\theta$ ) for TE and TM modes are demonstrated. The polarisation insensitivity TE and TM mode and absorption behaviors of the proposed MA are investigated by shifting the oblique angle incidences from  $0^\circ$  to  $90^\circ$  in Figs. 9(a, and b), respectively. The designed MA achieves a unique absorption properties for polarisation incident angle ( $\varphi$ ) up to  $90^\circ$  due to the axial and rotating symmetry. The absorption behavior of different oblique incident angle ( $\theta$ ) stability for the designed MA is illustrated in Figs. 10(a and b) for TE and TM modes, respectively.

In TE mode, the electric field ( $\vec{E}$ ) and the magnetic field ( $\vec{H}$ ) propagate through the x-axis, and z-axis, respectively. On the other hand, in TM mode, the electric field ( $\vec{E}$ ), and magnetic field ( $\vec{H}$ ) with the direction of x- the axis and y-axis, respectively. The absorption properties of  $0^\circ$  to  $60^\circ$  Oblique incident angle are listed in Table 2.

Table 2 and Fig. 10 shows that in TE mode, as the oblique incident angles increase from  $0^\circ$  to  $45^\circ$ , the average absorption and peak absorption are increased. On the other hand, from  $45^\circ$

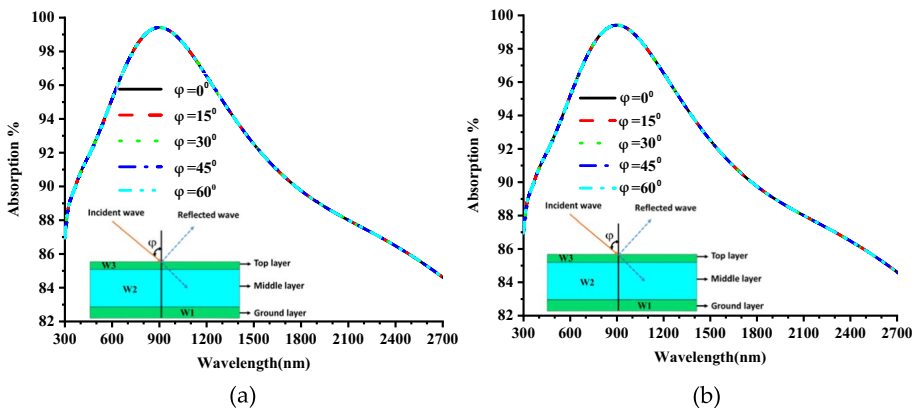


**Fig. 9** Polarisation insensitivity of **a** TE mode and **b** TM mode

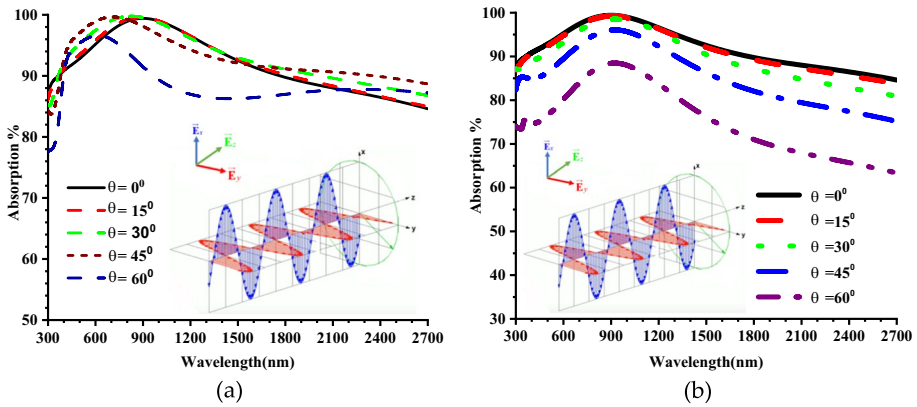


Fig. 10 Oblique incident angle stability **a** TE mode, **b** TM mode

**Table 2** Absorption characteristic of different oblique incident angle theta ( $\theta$ )

Oblique incident angle	TE mode		TM mode	
	Average absorption (%)	Peak absorption (%)	Average absorption (%)	Peak absorption (%)
0°	92.86	99.41	92.86	99.41
15°	93	99.54	92.46	99.25
30°	93.49	99.77	91.15	98.51
45°	93.32	99.64	87.53	96.07
60°	89	96.62	77.82	88.47

to 60°, the average and peak absorption values keep decreasing simultaneously. The maximum average and peak absorption are observed in 30° oblique incident angles. Likewise, in TM mode, as the oblique incident angles increase from 0° to 60, the average absorption and peak absorption have decreased. The highest average and peak absorption are noticed in 0° oblique incident angles.

### 3.4 Electric field, magnetic field, surface current, and temperature distributions

On the way to clarify the physical structure of the designed MA, the electric field ( $\vec{E}$ ), magnetic field ( $\vec{H}$ ), and surface current distribution (SCD) have been analyzed. Moreover, the EF, MF, and surface current are examined as different operating wavelengths. Moreover, the EF, MF, and SCD are calculated by using Maxwell equations. Hence, the fluctuating electric charge causes a rise in the electric field in front of it and a reduction in the electric field on the flip side of it, and these modifications create a strong magnetic field. The fluctuation of the magnetic field depends on the electric field concerning time and vice versa. The electric field and magnetic field are calculated by Eqs. (14) and (15), respectively (Saadat-Safa et al. 2019).

$$D_{\text{avg}} = \epsilon_{\text{eff}} \epsilon_0 E_{\text{avg}} \tag{14}$$

$$B_{\text{avg}} = \mu_{\text{eff}} \mu_0 H_{\text{avg}} \quad (15)$$

where  $D_{\text{avg}}$  is electric flux density,  $\epsilon_0$  is free space permittivity,  $\epsilon_{\text{eff}}$  is effective permittivity,  $E_{\text{avg}}$  is electric field density,  $B_{\text{avg}}$  is magnetic flux-density,  $\mu_0$  is free space permeability,  $\mu_{\text{eff}}$  is effective permeability,  $H_{\text{avg}}$  is magnetic field density. The flux densities related to the H and E field can be calculated through Maxwell integral Eqs. (16) and (17).

$$\int_C H \cdot dl = 0 + \frac{\partial}{\partial t} \iint_S D \cdot ds \quad (16)$$

$$\int_C E \cdot dl = 0 - \frac{\partial}{\partial t} \iint_S B \cdot ds \quad (17)$$

where E and H denote electric field intensity and magnetic field density, respectively. On the other hand, B indicates magnetic flux density and D denotes electric flux density. The integral equations are calculated with the surface or when the magnetic field illustrates non-uniform fluctuations rapidly shift after passing through electromagnetic wave propagation. Normally, the permittivity grasps unity in a constant field distribution, but, in this circumstance, H and B are asymmetric as well as non-uniform and hence the resulting electromagnetic wave propagates. At the resonance wavelength, the EF and HF distributions specify the relevant enormous concentration in certain specific areas of the upper surface. On the other hand, the surface current density is defined as the flow of charge through any cross-section of the conductor. This current density creates a magnetic field. With a stronger current density, the intensity of the magnetic field also increases. From the definition of the current density can be represented as Eq. (18).

$$J = \frac{d^2 I}{d^2 A} \quad (18)$$

The current density can be calculated by Eq. (19) (Parazzini et al. 2011).

$$J = \sigma \times E \quad (19)$$

where J is current density,  $\sigma$  is conductivity, and E is the electric field.

In Figs. 11(a, and b), the electric field (EF), and magnetic field (HF), is analyzed at 300 nm, 1550 nm, and 2800 nm wavelengths in both TE and TM modes, respectively. Figure 11a, it demonstrates that the electric field is mainly sited among the top of metallic patches and dielectric layer parts, particularly at the top and bottom margins of every resonator slide for (TE) polarisation and also for (TM). The red color represents the intense electric field. Yellow indicates quite dense regions, whereas blue represents minor packed regions. Figure 11b it can clearly understand that the shape of the metasurface is responsible for the resonance consequence. There are some methods for EM extension that are constrained with the help of boundary conditions on the magnetic field intensity. The incident ray that enters the designed unit cell is reflected in the ground and the resonant metal. Thus, EM waves are mainly confined to dielectric spacers. These blockaded plasmons create strong HF. The red color represents the most intense HF. The yellow and green represent soberly dense zones. However, the blue represents less packed zones. In Fig. 12a, surface current distribution is observed. The most current distribution is represented by red; yellow and green denote less. Figure 12b

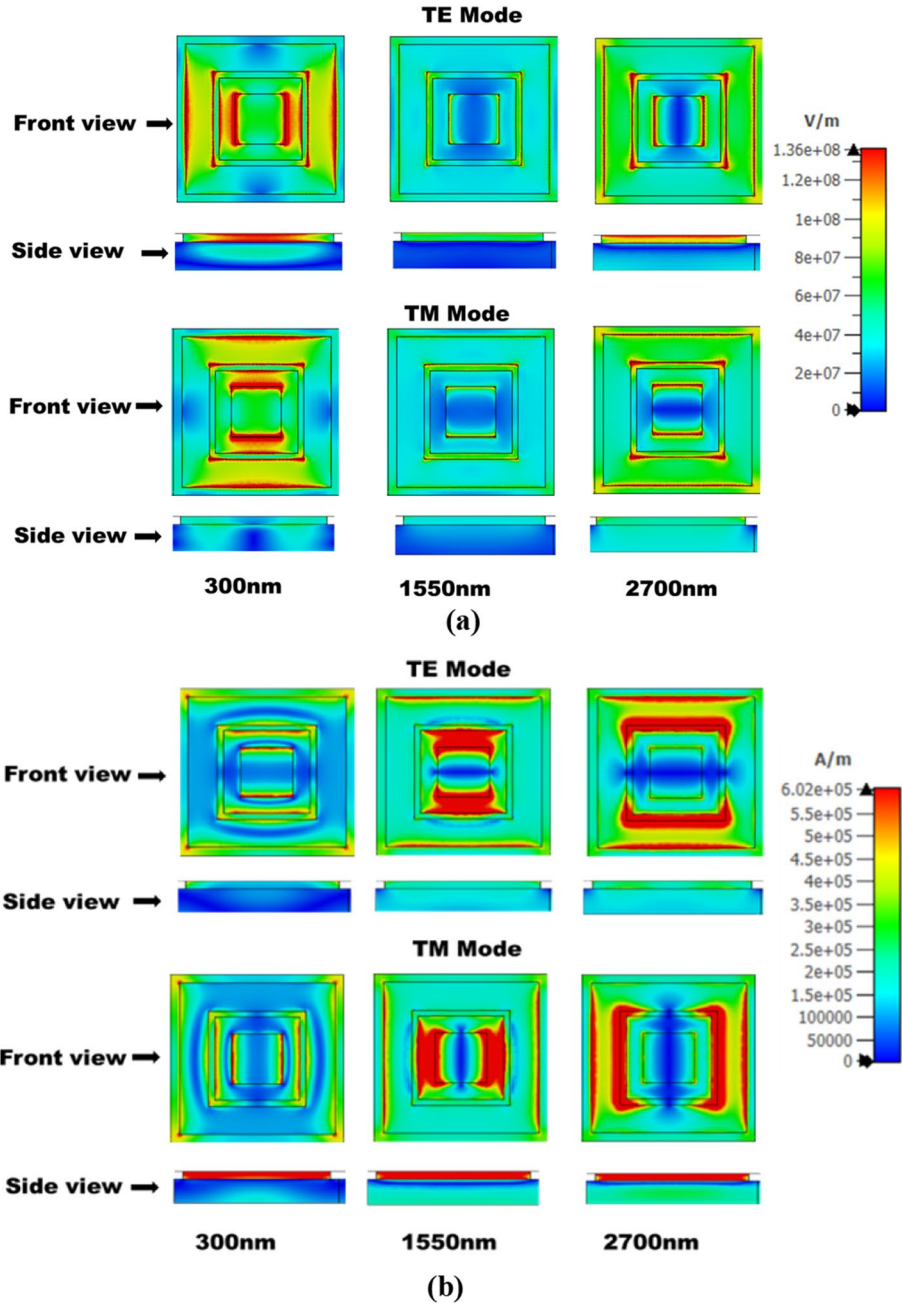
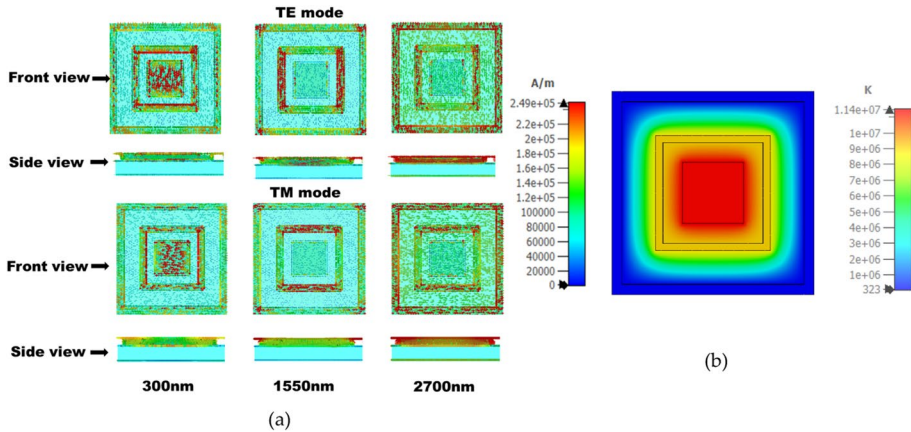


Fig. 11 **a** The electric field of proposed MA at TE and TM mode, **b** the magnetic field of proposed MA TE and, TM mode



**Fig. 12** **a** the surface current distribution of proposed MA at TE and TM mode, and **b** temperature distributions

shows the temperature distribution on the metallic surface of the MA in the Kelvin scale. From Fig. 11 a, b and Fig. 12 a, it is observed that the metallic cube resonator in the center experiences the most EM excitation and temperature change. This coherent relation can be explained by the Stefan-Boltzmann law (Wellons 2007). The temperature of the absorber is directly proportional to the intensity of the electromagnetic field density, according to the Stefan-Boltzmann law, which states that the total energy radiated by a blackbody is proportional to the fourth power of its absolute temperature.

Therefore, when an optical metamaterial absorber is exposed to light, it absorbs some of the electromagnetic energy and converts it into heat. This heat causes the temperature of the absorber to increase, which affects its optical properties. As the electromagnetic field density increases, the amount of absorbed energy increases, causing the temperature of the absorber to increase. This temperature change can also affect the dielectric constant of the material. The temperature dependence of the dielectric constant can be described using a mathematical model such as the Debye equation (Martin et al. 1971). The Debye equation is an empirical relationship that describes the dielectric constant of a material as a function of temperature and frequency. It takes the form of Eq. (20) (Sheng et al. 2013).

$$\epsilon(T) = \epsilon_h + \frac{(\epsilon_s - \epsilon_h)}{1 + (i\omega\tau(T))^\beta} \quad (20)$$

In Eq. (20),  $\epsilon(T)$  is the dielectric constant of the material as a function of temperature  $T$ ,  $\epsilon_h$  is the dielectric constant at high frequencies, where the polarization response of the material is negligible,  $\epsilon_s$  is the static dielectric constant, which describes the long-term polarization response of the material,  $\omega$  is the angular frequency of the electromagnetic field  $\tau(T)$  is the relaxation time, which describes the time it takes for the polarization response of the material to decay to a negligible level,  $i$  is the imaginary unit and  $\beta$  is an empirical parameter that describes the shape of the frequency dependence of the dielectric constant. Now using Eq. (20), the electric field Eqs. (14) can be rewritten as (21). Similarly, the magnetic field Eq. (15) can be rewritten as Eq. (22). These equations show that the electric and magnetic flux densities are proportional to the electric and magnetic field

intensities, respectively, and are also dependent on the temperature-dependent dielectric constant and magnetic permeability of the material.

$$D_{\text{avg}} = \epsilon(T)\epsilon_0 E_{\text{avg}} \tag{21}$$

$$B_{\text{avg}} = \mu(T)\mu_0 H_{\text{avg}} \tag{22}$$

The temperature dependence of  $\epsilon(T)$  and  $\mu(T)$  can be modelled using empirical equations or experimental data and may be influenced by various factors such as the material composition, structure, and frequency of the electromagnetic field.

### 3.5 Bending Effect of MA

The proposed MA sheet may have some exterior effects that can appear throughout the installation and maintenance levels (Hakim et al. 2022b). The complete structure is bent together from  $-16^\circ$  to  $16^\circ$  with  $4^\circ$  intervals. Convex bending (negative bending) and concave bending (positive bending) are demonstrated and analyzed. These two bendings are adept with the designed unit cell for flexible stress and firmness. Figures 13 (a, and b) show the result of convex and concave bending, respectively. It can be seen that the rate of absorption decreases with the bending angle increased. With the increased bend angle, the space of the top layer patch gets reduced. As a result, the resonant frequency ( $f_R$ ) has increased. The resonant frequency is determined by  $f_R = 1/(2\pi\sqrt{LC})$ . Where C and L indicate capacitance and inductance, respectively. For different bending angles, the average and peak absorption are listed in Table 3.

### 4 Comparative study of the existing design

Table 4 shows a detailed comparison of state-of-the-art research and the present designed MA. The comparison is based on used materials, dimensions, operating wavelength, average absorption, maximum absorption, bandwidth, MA configuration and oblique incident angle independence, etc. The MA presented in Hakim et al. 2022a; Chen et al. 2023) are

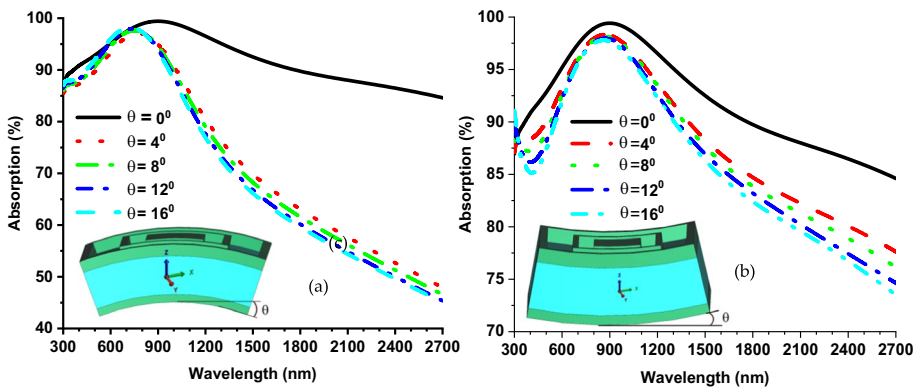


Fig. 13 Bending effects under a convex stress and, b concave stress



**Table 3** Absorption properties of various negative (convex) and positive (concave) bending angles

Bending angle	Convex bending		Concave bending	
	Average absorption (%)	Peak absorption (%)	Average absorption (%)	Peak absorption (%)
0°	94.42	99.41	94.42	99.41
4°	88.62	97.09	90.61	98.32
8°	88.85	97.63	89.97	98.11
12°	88.91	97.94	89.46	97.95
16°	89.08	98.23	89.05	97.79

presented for visible optical wavelengths absorption using dual resonators. Consequently, the MA in Zhang et al. (2021); Musa et al. 2022; Li et al. 2022) are designed for both visible and infrared regions, where multilayer approach is utilized for the wide absorption bandwidth. On the other hand, the proposed single layer square enclosed square resonators (SESR) structure forms strong EM coupling to achieve broad and high absorption bandwidth from visible to infrared wavelength, which is a significant contribution with respect to reported works. In addition, the proposed SESR structure shows higher oblique incident angle stability than (Chen et al. 2023; Musa et al. 2022; Li et al. 2022) and higher average absorption than (Hakim et al. 2022a; Chen et al. 2023) (Li et al. 2022). The average absorption of the designed SESR metamaterial achieves 94.47% (360–1750 nm), and the peak absorption is 99.77% at 900 nm. The designed SESR is smaller than the others listed MA in Table 4, which increases the absorption efficiency over a particular size of the MA plane. Moreover, the absorption characteristics of various banding conditions are also analyzed. Finally, the improved average absorption in wide operational bandwidth, wide oblique incident angle stability, polarization insensitivity, and bendable properties, make the proposed MA a potential candidate for visible and infrared regime applications.

## 5 Conclusions

In brief, a Ni-SiO<sub>2</sub>-based MA is designed and investigated with polarisation-insensitive and oblique incident angle stability for visible and optical window applications. The proposed MA is investigated by studying the electric field, magnetic field, and surface current density at the resonance absorption wavelength. The MA has achieved an average of 94.47% from 360 to 1780 nm and a peak of 99.47% at 900 nm. The MA shows oblique incident angle stability up to 60° for both TE and TM modes. The wide bandwidth with high absorption and bendable properties makes the proposed MA suitable for solar energy harvesting, photodetector, light trapping, etc.

**Table 4** Comparison with existing MMA

Ref	Structure materials	Absorption > 90% nm	Dimension (l × w × h) nm <sup>3</sup>	Wide-angle independency	Average absorption	Peak absorption	Polarisation independence	Bending investigation
Hakim et al. (2022a)	W, SiO <sub>2</sub>	380–750	950 × 950 × 240.13	0 ≤ 60°	92.2%	99%	Yes	Yes
Chen et al. (2023)	A-Si, Ag, ITO	300–680	1555 × 1555 × 560	0 ≤ 50°	> 90.1%	99%	Yes	N/A
Zhang et al. (2021)	Al-MgF <sub>2</sub> -Ti-SiO <sub>2</sub>	405–1505	380 × 380 × 415	0 ≤ 60°	95.14%	99%	Yes	N/A
Musa et al. (2022)	Tungsten, SiO <sub>2</sub>	350–1250	200 × 200 × 206.59	0 ≤ 45°	95.3%	98.2%	Yes	N/A
Li et al. (2022)	Ti-SiO <sub>2</sub>	250–1600	250 × 250 × 250	0 ≤ 45°	> 90%	N/A	Yes	N/A
Proposed	Ni-SiO <sub>2</sub>	360–1750	200 × 200 × 75	0 ≤ 60°	94.47%	99%	Yes	Yes

\*N/A-Not Acknowledged

**Acknowledgements** The authors are grateful to Universiti Kebangsaan Malaysia.

**Author contribution** Conceptualization, MBB, MLH, TA and MTI; Methodology, MBB, MLH, AFA, TA and MTI; Software, MLH; Validation, MBB, TA and MTI; Formal analysis, MBB, MSS, MLH, TA and MTI; Investigation, MBB, MLH, TA and MTI; Writing—original draft, MBB; Writing—review AND editing, MLH, AFA, MSS, TA, MTI, NM; Visualization, MBB and MLH; Supervision, TA and MTI; Funding acquisition, MTI.

**Funding** The authors acknowledge the Geran Universiti Penyelidikan (GUP), grant number GUP-2022–017 funded by the Universiti Kebangsaan Malaysia.

**Data availability** The data presented in this study are presented in this article.

## Declarations

**Conflict of interest** The authors declare no conflict of interest.

## References

- Alam, T., et al.: Metamaterial array based meander line planar antenna for cube satellite communication. *Sci. Rep.* **11**(1), 1–12 (2021)
- Bazgir, M., et al.: Highly Q-factor refractive index sensor based on graphene stack. *Optik* **268**, 169811 (2022)
- Bazgir, M. et al.: The Nano aperture in optical regime for bio-sensing, metasurface, and energy harvesting application: technical review. *Sens. Actuat. A Phys.*, p. 114495 (2023)
- Bilal, R., et al.: Elliptical metallic rings-shaped fractal metamaterial absorber in the visible regime. *Sci. Rep.* **10**(1), 1–12 (2020)
- Bilal, R., et al.: Polarization-controllable and angle-insensitive multiband Yagi-Uda-shaped metamaterial absorber in the microwave regime. *Opt. Mater. Exp.* **12**(2), 798–810 (2022)
- Byrnes, S.J., Blanchard, R., Capasso, F.: Harvesting renewable energy from Earth's mid-infrared emissions. *Proc. Natl. Acad. Sci.* **111**(11), 3927–3932 (2014)
- Carrillo, S.G.-C., et al.: Design of practicable phase-change metadevices for near-infrared absorber and modulator applications. *Opt. Exp.* **24**(12), 13563–13573 (2016)
- Cen, C., et al.: High quality factor, high sensitivity metamaterial graphene—perfect absorber based on critical coupling theory and impedance matching. *Nanomaterials* **10**(1), 1–12 (2020)
- Chen, X., et al.: Robust method to retrieve the constitutive effective parameters of metamaterials. *Phys. Rev. E* **70**(1), 016608 (2004)
- Chen, H.-Y., et al.: Broadband perfect polarization conversion metasurfaces. *Chin. Phys. B* **24**(1), 014201 (2015)
- Chen, D., et al.: Ultra-broadband dual-square ring metamaterial absorbers from visible to far-infrared region. *Optics Communications* **530**, 129124 (2023)
- CST Studio Suite. Available in <https://www.3ds.com/products-services/simulia/products/cst-studio-suite/> (accessed on 23 January 2023)
- Dash, R., et al.: Realization of 'non-linear invisibility cloak' using meta-material. *Optik* **127**(20), 9635–9639 (2016)
- Ding, F., et al.: Ultra-broadband microwave metamaterial absorber. *Appl. Phys. Lett.* **100**(10), 103506 (2012)
- Farmani, A., et al.: Highly sensitive nano-scale plasmonic biosensor utilizing Fano resonance metasurface in THz range: numerical study. *Physica E* **104**, 233–240 (2018)
- Garrison, J.D.: An electroplated nickel selective absorber. *Solar Energy Materials* **9**(4), 483–492 (1984)
- Hakim, M. et al.: Frequency integration of dual-band hexagonal metamaterial resonator antenna for Wi-Fi and 5G wireless communication. *J. Phys. Conf. Ser. IOP Publishing*, **2250**, 1–9 (2022)
- Hakim, M.L., et al.: Wide-oblique-incident-angle stable polarization-insensitive ultra-wideband metamaterial perfect absorber for visible optical wavelength applications. *Materials* **15**(6), 2201 (2022a)
- Hakim, M.L., et al.: Quad-band polarization-insensitive square split-ring resonator (SSRR) with an inner Jerusalem cross metamaterial absorber for Ku- and K-Band sensing applications. *Sensors* **22**(12), 4489 (2022b)

- Karthikeyan, M., et al.: Tunable optimal dual band metamaterial absorber for high sensitivity THz refractive index sensing. *Nanomaterials* **12**(15), 1–11 (2022)
- Kumar, R., Singh, B.K., Pandey, P.C.: Broadband metamaterial absorber in the visible region using a petal-shaped resonator for solar cell applications. *Phys. E Low Dimension. Syst. Nanostruct.*, p. 115327 (2022)
- Landy, N.I., et al.: Perfect metamaterial absorber. *Phys. Rev. Lett.* **100**(20), 207402 (2008)
- Li, F., et al.: Polarization-dependent wideband metamaterial absorber for ultraviolet to near-infrared spectral range applications. *Opt. Express* **30**(15), 25974–25984 (2022)
- Liu, J., et al.: A metamaterial absorber based on particle swarm optimization suitable for earth's atmospheric transparency window. *IEEE Access* **9**, 92941–92951 (2021)
- Martin, A.J., Meier, G., Saupe, A.: Extended Debye theory for dielectric relaxations in nematic liquid crystals. In: *Symposia of the Faraday Society*. Royal Society of Chemistry (1971)
- Mehrabi, S., Rezaei, M.H., Zarifkar, A.: Ultra-broadband solar absorber based on multi-layer TiN/TiO<sub>2</sub> structure with near-unity absorption. *JOSA B* **36**(9), 2602–2609 (2019)
- Misran, N., et al.: Analysis of parameterization substrate thickness and permittivity for concentric split ring square reflectarray element. *Jurnal Kejuruteraan (journal of Engineering)* **23**, 11–16 (2012)
- Mobasser, S., et al.: Highly sensitive reconfigurable plasmonic metasurface with dual-band response for optical sensing and switching in the mid-infrared spectrum. *J. Electron. Mater.* **50**, 120–128 (2021)
- Musa, A., et al.: Polarization independent metamaterial absorber with anti-reflection coating nanoarchitectonics for visible and infrared window applications. *Materials* **15**(10), 1–16 (2022)
- Naveed, M.A., et al.: Ultrawideband fractal metamaterial absorber made of nickel operating in the UV to IR spectrum. *Opt. Express* **29**(26), 42911–42923 (2021)
- Ning, J., et al.: An Ultrathin Tunable Metamaterial Absorber for Lower Microwave Band Based on Magnetic Nanomaterial. *Nanomaterials* **12**(13), 1–14 (2022)
- Parazzini, M., et al.: Transcranial direct current stimulation: estimation of the electric field and of the current density in an anatomical human head model. *IEEE Trans. Biomed. Eng.* **58**(6), 1773–1780 (2011)
- Ponizovskaya Devine, E.: Mid-infrared photodetector based on 2D material metamaterial with negative index properties for a wide range of angles near vertical illumination. *Appl. Phys. A* **127**(3), 1–5 (2021)
- Poorgholam-Khanjari, S., Zarrabi, F.B.: Reconfigurable Vivaldi THz antenna based on graphene load as hyperbolic metamaterial for skin cancer spectroscopy. *Optics Communications* **480**, 126482 (2021)
- Razavi, Z., Zarrabi, F.B.: Developing Plasmonic Perfect thin-film absorber by studying self-similar formation to have Fano response for optical spectroscopy. *Optics Commun.* **504**, 127495 (2022)
- Rothwell, E.J., et al.: Analysis of the Nicolson-Ross-Weir method for characterizing the electromagnetic properties of engineered materials. *Prog. Electromagnet. Res.* **157**, 31–47 (2016)
- Saadat-Safa, M., et al.: A CSRR-based sensor for full characterization of magneto-dielectric materials. *IEEE Trans. Microw. Theory Tech.* **67**(2), 806–814 (2019)
- Sheng, J., et al.: Temperature dependence of the dielectric constant of acrylic dielectric elastomer. *Appl. Phys. A* **110**, 511–515 (2013)
- Shuvo, M.M.K., et al.: A wide-angle, enhanced oblique incidence, bend-able metamaterial absorber employed in visible region with a sun shape resonator. *IEEE Access* **9**, 126466–126480 (2021)
- Smith, D., et al.: Determination of effective permittivity and permeability of metamaterials from reflection and transmission coefficients. *Phys. Rev. B* **65**(19), 195104 (2002)
- Tang, P., et al.: Plasmonic wavy surface for ultrathin semiconductor black absorbers. *Opt. Express* **28**(19), 27764–27773 (2020)
- Tang, W., Chen, J., Cui, T.J.: Metamaterial lenses and their applications at microwave frequencies. *Adv. Photon. Res.* **2**(10), 2100001 (2021)
- Tian, X., et al.: UV-visible broadband polarization-independent metamaterial absorber based on two-dimensional Au grating. *Opt. Laser Technol.* **157**, 108729 (2023)
- Wellons, M.: The Stefan-Boltzmann Law. *Physics Department, The College of Wooster, Wooster, Ohio*, **44691**, p. 25 (2007)
- Xiao, Z.-Y., et al.: Multi-band transmissions of chiral metamaterials based on Fabry-Perot like resonators. *Opt. Exp.* **23**(6), 7053–7061 (2015)
- Xiong, Y., et al.: Ultra-thin optically transparent broadband microwave metamaterial absorber based on indium tin oxide. *Opt. Mater.* **132**, 112745 (2022)
- Yin, X., et al.: Ultra-wideband microwave absorber by connecting multiple absorption bands of two different-sized hyperbolic metamaterial waveguide arrays. *Sci. Rep.* **5**(1), 1–8 (2015)
- Zarrabi, F.B., Bazgir, M., Hekmati, R.: Reconfigurable optical Heptamer disk absorber based on an optical switch. *IEEE Photonics Technol. Lett.* **31**(10), 779–782 (2019)

Zhang, C., et al.: Design and analysis of a broadband metamaterial absorber applied to visible light band. *Opt. Mater.* **121**, 111533 (2021)

**Publisher's Note** Springer Nature remains neutral with regard to jurisdictional claims in published maps and institutional affiliations.

Springer Nature or its licensor (e.g. a society or other partner) holds exclusive rights to this article under a publishing agreement with the author(s) or other rightsholder(s); author self-archiving of the accepted manuscript version of this article is solely governed by the terms of such publishing agreement and applicable law.